Phys. Status Solidi B **248**, No. 2, 375–383 (2011) / **DOI** 10.1002/pssb.201000634

physica status solidi b
www.pss-b.com
basic solid state physics

Feature Article

Quantum-dot excitons in nanostructured environments

Jørn M. Hvam*, Søren Stobbe, and Peter Lodahl

DTU Fotonik, Department of Photonics Engineering, Technical University of Denmark, 2800 Kgs. Lyngby, Denmark

Received 7 July 2010, accepted 4 October 2010
Published online 9 November 2010

Keywords oscillator strength, photonic crystals, quantum-dot excitons, spin-flip

* Corresponding author: e-mail jmhv@fotonik.dtu.dk, Phone: +45 4525 5758, Fax: +45 4593 6581

The interaction between light and quantum-dot (QD) excitons is strongly influenced by the environment in which the QD is placed. We have investigated the interaction by measuring the time-resolved spontaneous-emission rate of QD excitons in different nanostructured environments. Thereby, we have determined the oscillator strength, quantum efficiency and spin-flip rates of QD excitons as well as their dependencies on emission wavelength and QD size. Enhancement and inhibition of QD spontaneous emission in photonic crystal membranes (PCMs) is observed. Efficient coupling to PCM waveguides is demonstrated and the influence of disorder is discussed. The findings have a strong bearing on future nanophotonic devices.

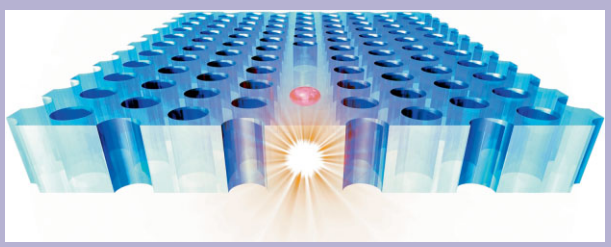

QD emitter placed in a photonic crystal membrane waveguide (artist's view).

1 Introduction The interaction between excitons and light, as *e.g.* manifested by the spontaneous emission rate, is essentially governed by two factors: The oscillator strength which describes the strength of the exciton–photon interaction, as can be calculated on a quantum-mechanical basis [1], and the density of optical states (DOS) to interact with [2]. The latter can be calculated classically from Maxwell's equations once the material environment is specified.

In the weak-coupling limit the light–matter interaction strength can be calculated perturbatively leading to Fermi's golden rule. In the strong-coupling limit, the full exciton–photon Hamiltonian is diagonalised leading to a new quasi particle the (exciton-)polariton [3] with a mixed exciton/photon character depending on the detuning from the bare exciton resonance. Prominent examples of strong coupling are (Wannier) exciton-polaritons in bulk wide-gap II–VI semiconductors [4] and cavity-polaritons in III–V semiconductor microcavities [5]. Recently, strong coupling has also been observed between single quantum-dot (QD) excitons and various types of nanocavities [6, 7]. The latter two cases are examples showing that strong coupling can also be achieved by modifying the local density of optical states (LDOS) through micro/nano-structuring the refractive index of the surrounding material, *e.g.* by forming nanocavities with high quality factors (Q) and small mode volumes.

Single or few QDs coupled to micro or nanocavities have been the subject of intense studies in recent years [8]. The interest has been spurred by the potential application of QDs and nanocavities for low threshold (low energy) lasers [9], switches [10] and other optoelectronic devices, including also emerging and future devices for quantum information processing [11, 12]. One key challenge is the technology of the QD growth in order to control the composition, size, shape and positioning with respect to the nanocavities [7, 13]. Furthermore, the fundamental properties of QD excitons and their coupling to nanocavities and their distinction from atomic systems start to be appreciated [14, 15].

The oscillator strength of QD excitons can in principle be determined from an absorption experiment [16]. However, this is virtually impossible to perform on a single QD and very difficult on small ensembles of QDs. Alternatively, it can be determined from the decay rate of spontaneous emission provided the nonradiative decay rate, or the internal quantum efficiency, is precisely known [17].

In the present paper we will focus our attention on the study of spontaneous emission from QD excitons in various nanostructured environments. In the first part (Section 3), we will make use of a modified LDOS to determine fundamental QD exciton parameters like quantum efficiency, oscillator strength [17, 18] and spin-flip rates [19]. In the second part (Section 4), we will demonstrate how one can modify and control the spontaneous emission rate [20, 21], by operating in the weak-coupling limit, into specific optical modes [22] by proper structuring of the immediate surroundings of the QD excitons. The investigations are of fundamental character and are considered as prerequisites to venture further into all-solid-state quantum optics/photonics with applications in future integrated optics and nanophotonics including single-photon devices for quantum communication and quantum computing [11, 12].

2 Experimental

2.1 Self-assembled quantum dots The QDs investigated here are self-assembled Stranskii–Krastanov InAs/GaAs or $In_xGa_{1-x}As$/GaAs dots grown by molecular beam epitaxy on (001) oriented GaAs substrates as described in detail in Refs.[17, 18]. The InAs dots are typically relatively small, around 20 nm in diameter and with average height of about 7 nm, with a significant spread giving rise to an inhomogeneous broadening of 60–80 meV of the ground-state transition from an ensemble of these QDs. The areal density of the InAs QDs, as determined by atomic force microscopy (AFM), is typically 250 μm^{-2}, corresponding to an average distance of 60 nm between QDs. This excludes any significant interaction between QDs so that all measurements can be considered ensemble-averaged values of the properties of individual QDs. The $In_xGa_{1-x}As$ ($x = 0.3$) QDs are typically larger, 40–70 nm in diameter, with a correspondingly lower areal density of 100 μm^{-2}.

2.2 Interface and photonic crystal structures The single layer of QDs described above are embedded in layers of GaAs and AlAs allowing for further processing of samples to be investigated. For interface studies, the QD layer is overgrown by 300 nm of GaAs. The wafer was then processed by standard UV lithography and wet chemical etching in five subsequent steps with nominal etch depths of 160, 80, 40, 20, and 10 nm by which was obtained 32 fields with specific distances (spaced by 10 nm) from the QDs to the semiconductor surface (see Ref. [17] for further details). A schematic illustration of the resulting sample is shown in Fig. 1(a).

For photonic crystal studies, a sacrificial layer of AlAs is first grown followed by a 150-nm layer of GaAs with a single layer of InAs self-assembled QDs in the centre. The photonic crystal structures are then formed by electron-beam lithography and dry etching followed by wet etching of the sacrificial AlAs layer to form the photonic crystal membrane (PCM). The PCM consists of holes arranged in a triangular lattice with hole radius r and lattice constant a and a fill factor around 66% ($r/a \sim 0.3$), see details in Refs. [21, 22]. In the PCM a photonic crystal waveguide (PCW) can be formed by omitting one row of holes (W1 waveguide). In Fig. 1(b) is shown a SEM picture of a typical PCM with a W1 waveguide.

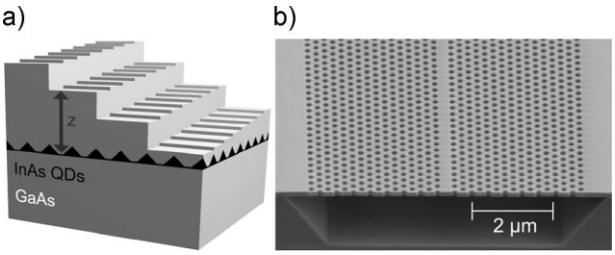

Figure 1 (a) Schematic drawing of the interface sample; (b) SEM picture of photonic crystal membrane with W1 waveguide.

2.3 Optical characterisation The QD excitons have been studied by time-resolved micro-photoluminescence (μ-PL). The samples were placed in a helium flow cryostat mounted on precision translational stages and excited by subpicosecond or picosecond pulses from a mode-locked Ti:sapphire laser with a repetition rate of 78 MHz and emitting at around 800 nm. The excitation spot size could be varied from >100 μm down to 1.4 μm, which is also the ultimate spatial resolution of the emission which is sent through a spectrometer and detected by either a CCD camera for recording full spectra or an avalanche photodiode (APD) for time-resolved measurement, see Fig. 2. Thus, both ensemble measurements and, by combining spatial and spectral resolution, single-dot PL measurements can be performed with a time resolution down to 40 ps. All experiments are performed at cryogenic temperatures, normally around 10 K. Further details on the experimental techniques can be found in Refs. [17, 22].

3 Quantum-dot excitons

For excitons in QDs there are three different regimes of quantisation depending on the relative importance of the electron–hole Coulomb interaction and the quantisation energies of electrons and holes in the confining QD potential [23].

For small QDs with an average radius $R \ll a_x$, where a_x is the (bulk) exciton Bohr radius, the electron and hole

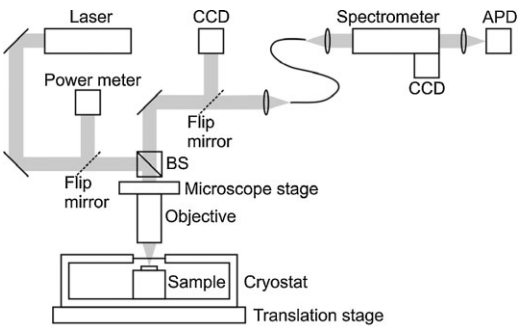

Figure 2 Schematics of the experimental setup. BS: beamsplitter; CCD: charge-coupled device/camera; APD: avalanche photo diode.

quantisation energies dominate over the Coulomb energy. In this so-called strong confinement (SC) limit, exciton effects are negligible and the oscillator strength can be expressed as [17, 18]

$$f_{\mathrm{SC}}(\omega) = \frac{E_{\mathrm{p}}}{\hbar\omega}\left|\langle F_{\mathrm{e}}(\omega) \mid F_{\mathrm{h}}(\omega)\rangle\right|^2 \leq \frac{E_{\mathrm{p}}}{\hbar\omega}, \tag{1}$$

where E_{p} is the Kane energy for the semiconductor constituting the QD, $\hbar\omega$ is the transition energy, and $F_{\mathrm{e(h)}}(\omega)$ is the envelope of the electron (hole) wavefunction.

For intermediate-sized QDs ($R \sim a_x$) where the Coulomb and quantisation energies have to be treated on an equal footing, there is no simple solution for the oscillator strength, whereas for large QDs, with $R \gg a_x$, the quantisation energies are small compared to the Coulomb energy. In this weak confinement (WC) limit, the exciton wavefunction is essentially unaltered by the confinement and only the translational energy of the exciton is quantised in the QD potential. Correspondingly, the oscillator strength is essentially the bulk exciton oscillator strength [24]

$$f_{\mathrm{WC}}(\omega) = f_x(\omega) = \frac{E_{\mathrm{p}}}{\hbar\omega}\frac{V_{\mathrm{coh}}}{\pi a_x^3} \leq \frac{E_{\mathrm{p}}}{\hbar\omega}\frac{V_{\mathrm{QD}}}{\pi a_x^3}, \tag{2}$$

where V_{coh} is the coherence volume of the exciton and V_{QD} is the volume of the QD.

Specifically, for $In_xGa_{1-x}As$ self-assembled QDs with $E_{\mathrm{p}} = E_{\mathrm{p}}(x) = (28.8 - 7.3x)$ eV, and assuming infinite barriers in the growth direction and a parabolic confinement potential in the plane perpendicular to it, one can obtain [25, 26]

$$f_{\mathrm{WC}}(\omega, x) \leq \frac{2E_{\mathrm{p}}(x)}{\hbar\omega}\left(\frac{L}{a_x}\right)^2, \tag{3}$$

where L is the diameter of the QD, defined as four standard deviations of the Gaussian centre-of-mass wavefunction. Thus, for large QDs there is the potential for "giant" oscillator strength [27] provided the exciton is coherent over the whole QD volume. It should also be mentioned that the above analysis assumes the dipole approximation to be valid for all QDs, which may not hold for large QDs.

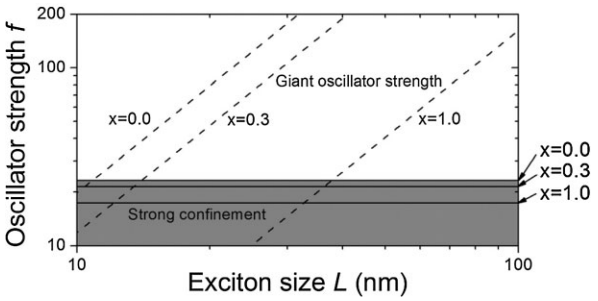

Figure 3 Calculated oscillator strength for $In_xGa_{1-x}As$ QDs with $x = 0$, $x = 0.3$ and $x = 1.0$. In the weak confinement limit (dashed lines) f_{WC} increases quadratically with the exciton (QD) size, whereas in the strong confinement limit $f_{\mathrm{SC}} \leq 23.2$ (17.1) for GaAs (InAs).

Applying Eqs. (1) and (3), the upper bounds for the oscillator strength are plotted in Fig. 3 in the SC (solid lines) and WC (dashed lines) limits, respectively for $In_xGa_{1-x}As$ QDs with $x = 0$, $x = 0.3$ and $x = 1.0$. Thus, oscillator strengths beyond 100 should be achievable in large $In_{0.3}Ga_{0.7}As$ QDs facilitating strong coupling between single large QDs and nanocavities.

Indeed strong coupling has been observed in such systems [6]. We have pursued a different route to directly determine the oscillator strength from the radiative decay rate of QD excitons in a nanostructured environment [17, 18].

3.1 Determination of oscillator strength The radiative recombination rate $\Gamma_{\mathrm{rad}}(\omega)$ of QD excitons in a homogeneous medium with refractive index n can be calculated from Fermi's golden rule and expressed by the oscillator strength $f_x(\omega)$ and the DOS $\rho_{\mathrm{hom}}(\omega) = n^3\omega^2/\pi^2c^3$ [18]

$$\Gamma_{\mathrm{rad}}(\omega) = \frac{\pi e^2 f_x(\omega)\rho_{\mathrm{hom}}(\omega)}{6\varepsilon_0 m_0 n^2} = \frac{ne^2\omega^2}{6\pi\varepsilon_0 m_0 c^3} f_x(\omega), \tag{4}$$

where ε_0, m_0 and c are the vacuum dielectric constant, the free electron mass, and the velocity of light in vacuum, respectively. However, in order to determine $\Gamma_{\mathrm{rad}}(\omega)$ from the PL decay of QD excitons after a short-pulse excitation one needs to know also the nonradiative decay rate $\Gamma_{\mathrm{nrad}}(\omega)$, *i.e.* the internal quantum efficiency

$$\eta_{\mathrm{int}}(\omega) = \frac{\Gamma_{\mathrm{rad}}(\omega)}{\Gamma_{\mathrm{rad}}(\omega) + \Gamma_{\mathrm{nrad}}(\omega)} = \frac{\Gamma_{\mathrm{rad}}(\omega)}{\Gamma(\omega)}. \tag{5}$$

The radiative and non-radiative recombination rates can be separated by measuring the decay rates of QD excitons placed at different positions $\mathbf{r}$ in an environment with a known LDOS $\rho_l(\omega,\mathbf{r})$ [28]. We have done this for the sample shown in Fig. 1(a), *i.e.* measured [17, 18]

$$\Gamma(\omega, z) = \Gamma_{\mathrm{rad}}(\omega)\frac{\rho_l(\omega, z)}{\rho_{\mathrm{hom}}(\omega)} + \Gamma_{\mathrm{nrad}}(\omega), \tag{6}$$

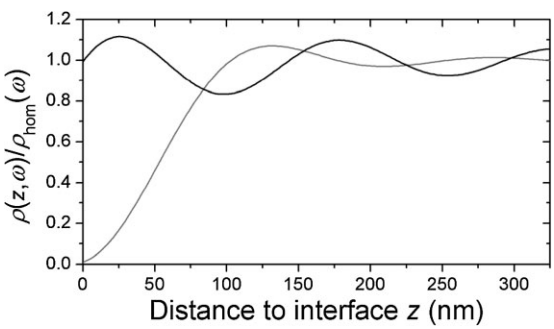

Figure 4 The LDOS as a function of distance z to a GaAs–air interface for a dipole oriented parallel (black curve) or perpendicular (grey curve) to the interface.

where $\rho_l(\omega,z)$ is the projection of the LDOS along the direction of the transition dipole moment of the QD exciton and shown in Fig. 4 as a function of the distance z to a GaAs–air interface for two dipole orientations parallel and perpendicular to the interface. For Stranskii–Krastanov grown InAs/GaAs QDs the transition dipole moment is oriented perpendicular to the growth direction, *i.e.* parallel to the GaAs–air interfaces of the sample sketched in Fig. 1(a).

Examples of measured PL decay curves are shown in the inset of Fig. 5(a) for two different distances from the interface. The decays are bi-exponential with a slow decay rate $\Gamma_s \sim 0.1\ \mathrm{ns}^{-1}$ and a fast decay rate Γ_f which is about one order of magnitude larger. The slow decay rate is largely independent of the distance to the surface as seen in the lower curve of Fig. 5(a). It is ascribed to the influence of the dark exciton states, as we will discuss in the next section.

The variation of the fast decay rate with the distance to the interface is shown as the upper curve in Fig. 5(a). The points are the measured decay rates and the solid curve is a fit by Eq. (6) with the known values of $\rho_l(\omega,z)$ and $\rho_{\mathrm{hom}}(\omega)$. The fit is excellent for distances $z > 100$ nm, and from this fit the radiative recombination rate $\Gamma_{\mathrm{rad}}(\omega)$ as well as the nonradiative recombination rate $\Gamma_{\mathrm{nrad}}(\omega)$ are uniquely determined without any further assumptions about the sample. The deviations for $z < 100$ nm could be related to dissipation at the sample surface [17], but do not influence the determination of the QD parameters.

The oscillator strength $f_x(\omega)$ and the internal quantum efficiency $\eta_{\mathrm{int}}(\omega)$ are determined by Eqs. (4) and (5), respectively. The results are shown in Fig. 6(a) as a function of transition energy across the inhomogeneously broadened

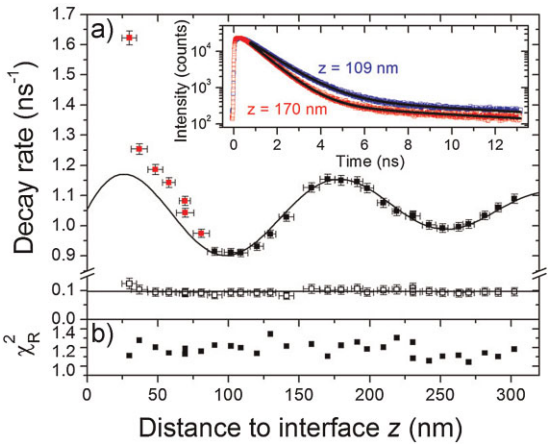

Figure 5 (online colour at: www.pss-b.com) (a) Measured decay rates as a function of distance z to the GaAs–air interface (solid squares). Calculated decay rates (solid curve) applying the LDOS projected onto a dipole oriented parallel to the interface. The inset shows PL decays for two different distances to the interface perfectly fitted by bi-exponential decays with $\Gamma_f = 0.91\ \mathrm{ns}^{-1}$ and $\Gamma_s = 0.09\ \mathrm{ns}^{-1}$ for $z = 109$ nm and $\Gamma_f = 1.15\ \mathrm{ns}^{-1}$ and $\Gamma_s = 0.10\ \mathrm{ns}^{-1}$ for $z = 170$ nm. (b) Goodness-of-fit χ^2_R for all distances to the interface.

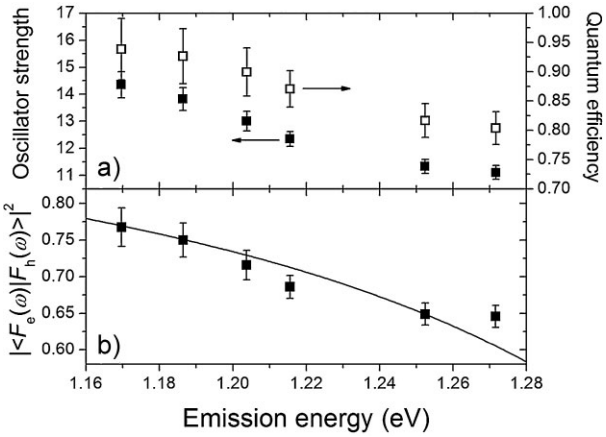

Figure 6 (a) Oscillator strength (solid squares, left scale) and quantum efficiency (open squares, right scale) versus emission photon energy. (b) Measured (squares) and calculated (solid curve) overlap of the envelope wavefunctions of electrons and holes.

PL spectrum from an ensemble of InAs/GaAs QD excitons [17]. The QDs examined in Fig. 6 are relatively small (diameter ~20 nm, height ~6 nm) whereby the excitons can be considered to be in the SC limit. Applying Eq. (1), we can then estimate the overlap integral of the electron and hole wavefunctions. The result is shown as experimental points in Fig. 6(b) and compared with a model calculation based on lens-shaped QDs with a size distribution giving rise to ground state transitions matching the inhomogeneously broadened PL spectrum [17]. More details of these experiments can be found in Refs. [17, 18].

It has been argued that oscillator strengths well beyond what is determined above are necessary to obtain strong coupling between a single QD and a high-Q nanocavity [29]. We have performed the above measurements also on $In_{0.3}Ga_{0.7}As$/GaAs QDs with a diameter of 40 nm which, according to Eq. (3), should give rise to an oscillator strength $f_{WC} > 100$ (Fig. 3). However, oscillator strengths in the same range as for the smaller QDs were found, but with a significantly lower quantum efficiency [26]. We may therefore conclude that the coherence volume (area) of the excitons in these QDs is smaller than the actual volume (area) of the QDs, *e.g.* by excitons being further localised by a fluctuating potential from strain and/or alloy disorder.

3.2 Dark excitons and spin-flip rates In the above analysis we neglected the slow part of the decay. However, the decay curves in Fig. 5(a) are fitted excellently with the bi-exponential function

$$I(t) = A_f e^{-\Gamma_f t} + A_s e^{-\Gamma_s t}, \tag{7}$$

where the fast and slow amplitudes, A_f and A_s, are included as parameters. With this additional information it is possible to gain further insight in the QD exciton dynamics, including the spin flips connecting the bright and dark

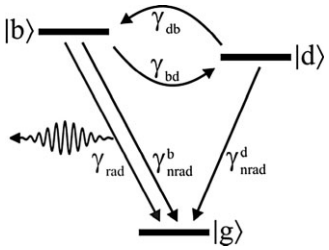

Figure 7 Exciton level scheme with bright, dark and ground states. The transition rates are indicated and explained in the text.

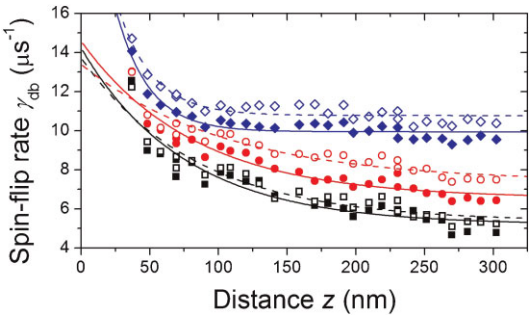

Figure 8 (online colour at: www.pss-b.com) The spin-flip rates as a function of distance z to the interface for different emission energies 1.170, 1.187, 1.204, 1.216, 1.252 and 1.272 eV counted from below at $z = 300$ nm. The solid curves are fits to the experimental points assuming an exponential decay of the rates away from the interface with characteristics lengths of 25–110 nm.

exciton states that are initially both populated after a short-pulse excitation into the continuum states.

Figure 7 shows the fine structure of the lowest exciton state for InAs/GaAs QDs. The exciton is formed by the conduction-band electron state (spin 1/2) and the heavy-hole valence-band state (total angular momentum 3/2). Thus, four exciton states can be formed characterised by the projections of the total angular momentum onto the growth axis with the values ± 1or $\pm 2$for bright and dark excitons, respectively. The bright-exciton level $|b\rangle$is typically a few hundred μeV above the dark-exciton level $|d\rangle$. The splitting is determined by the exchange coupling between electron and hole spins. The bright excitons can decay into the ground state $|g\rangle$ either radiatively (γ_{rad}) or nonradiatively$(\gamma^{b}_{\mathrm{nrad}})$. The dark excitons can only recombine nonradiatively $(\gamma^{d}_{\mathrm{nrad}})$. Alternatively, they can be transformed into bright excitons via a phonon-mediated spin-flip process with a rate γ_{db} [30, 31]. The reverse process may also occur with a rate γ_{bd}.

Assuming that the spin-flip rates are much slower than both radiative and nonradiative recombination rates, we can identify the decay rates $\Gamma_{\mathrm{f}} \cong \gamma_{\mathrm{rad}} + \gamma^{b}_{\mathrm{nrad}}$ and $\Gamma_{\mathrm{s}} \cong \gamma^{d}_{\mathrm{nrad}}$. Thus, the spin-flip rates cannot be determined directly from these decay rates. However, the amplitudes of the fast and slow components carry additional information including the spin-flip rates [19]:

$$\frac{A_{\mathrm{f}}(z)}{A_{\mathrm{s}}(z)} = \frac{\Gamma_{\mathrm{f}}(z) - \Gamma_{\mathrm{s}}(z)}{\gamma_{db}(z)} \frac{n_b(t=0)}{n_d(t=0)}, \tag{8}$$

where $n_{b/d}(t=0)$ are the initial populations of bright/dark excitons, which can be considered equal for very low density of non-resonant excitation. In our experiments, the excitation density was typically such that the initial average population was 0.1 exciton per QD. Thus, there is a finite probability to form biexcitons that will recombine radiatively and always leave bright excitons behind. This results in a slight overweight of bright excitons over dark excitons: $n_b(t=0)/n_d(t=0) \approx 1.25$ [19].

The spin-flip rate can then be determined from Eq. (8) and the result is shown in Fig. 8 as a function of distance to the interface and for different transition energies across the inhomogeneously broadened PL line [19]. As it turns out, the spin-flip rate increases in an exponential fashion when approaching the interface with a characteristic length of 25–110 nm. This length is comparable to the wavelength of acoustic phonons with energies matching the exchange splitting between bright and dark excitons. Thus, the increase could be caused by an enhancement of the acoustic phonons at the interface [19].

The spin-flip rate also depends strongly on the emission energy and thereby the QD size. The values furthest away from the interface are plotted in Fig. 9 as a function of emission energy and are seen to vary from 6 ns^{-1} at 1.170 eV to 13 ns^{-1} at 1.272 eV. A calculation of the spin-flip rate based on short-range exchange interaction and acoustic phonons [31] produce the same trend in energy dependence, but at rates that are two orders of magnitude lower (dashed curve in Fig. 9). This discrepancy can be reduced somewhat by varying the composition, size and shape of the QDs (solid curve in Fig. 9), but still without a perfect fit to the experimental results [19]. Thus additional processes are likely to contribute to the exciton spin flips in QDs.

4 Quantum-dots in photonic crystals In the above, we have studied the influence of very simple modifications of the QD environment. More dramatic changes of the light–matter interaction can be achieved in

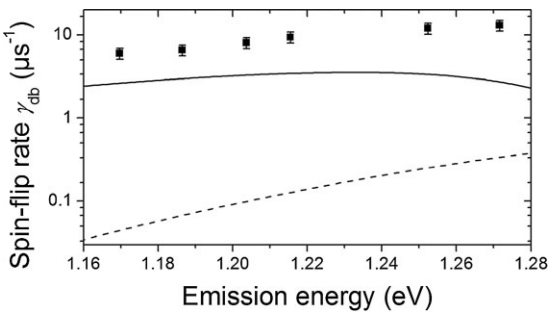

Figure 9 Measured spin-flip rates (solid squares) at different emission energies and far from the interface ($z = 302$ nm). The dashed curve is a model calculation reproducing the energy dependence of the radiative decay rate (Fig. 6) and the solid curve is calculated with parameters optimised to fit the measured spin-flip rates.

a photonic crystal environment where spontaneous emission from QD excitons can be strongly enhanced or inhibited depending on the emission energy in relation to the photonic band structure of the photonic crystal [20]. Here we will study the spontaneous emission rate of InAs/GaAs QD excitons embedded in a two-dimensional PCM as described in Section 2.2 [Fig. 1(b)]. It is of particular interest to study the emission rate in the spectral region in and around the band gap of the PCM [21].

Since the ground-state transition energy of QD excitons embedded in the membrane is relatively fixed, we prepared a series of PCMs with lattice constant a (pitch) ranging from 180 to 470 nm in steps of 10 nm and with constant fill factor $(r/a = 0.313 \pm 0.006)$. For the whole series, we then measured time resolved PL decay at a fixed wavelength ($\lambda = 980$ nm) after a short-pulse excitation at a fixed intensity into the GaAs barrier material [21].

The result is shown in Fig. 10, where we observe a pronounced slow down of the decay, indicating a strong inhibition of the spontaneous emission, in the region $0.26 \leq a/\lambda \leq 0.35$ for which the emission wavelength is within the band gap of the corresponding PCM. The PL decays in Fig. 10(a) are strongly non-exponential (multi-exponential) which is to be expected since the observed PL decay is an average over an ensemble of QDs with different positions and orientations within the PCM and thereby different LDOS. Still, we can define a mean decay time $\tau_m = \int_0^\infty tI(t)dt / \int_0^\infty I(t)dt$ to characterise the decay rates in Fig. 10(a). The corresponding mean decay rates τ_m^{-1} are plotted in Fig. 10(b) as solid squares and compared with a model calculation [32] shown as open squares. The measured reference decay rate is $\tau_m^{-1} = 0.75\,\mathrm{ns}^{-1}$ in the absence of the PCM. Thus, within the band gap we observe a sixfold reduction/inhibition of the decay rate, whereas an increase (up to 30%) of the decay rate is observed just outside the band gap. It should be noted that the measured decay rates include nonradiative decays that are unaffected by the variations in the LDOS.

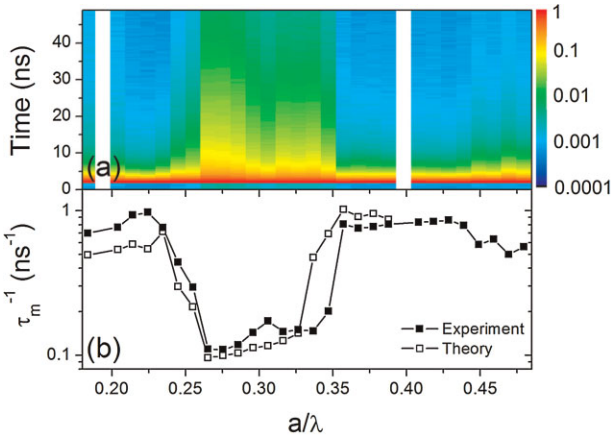

Figure 10 (online colour at: www.pss-b.com) (a) Colour-coded contour plots of normalised time-resolved decay curves and (b) extracted mean decay rates (solid squares) and simulated values (open squares) for different lattice constants normalised to the emission wavelength. The band-gap effect is clearly seen in the region $0.26 < a/\lambda < 0.35$.

These investigations serve as a background for further studies of the strong enhancement (Purcell effect) of QD exciton emission in particular nanocavity modes within the band gap of PCMs. In the weak-coupling limit for QDs in a micro/nanocavity two parameters are essential to describe the coupling efficiency. The Purcell factor F_p is the factor with which the spontaneous emission rate is enhanced in the cavity over the emission rate in a homogeneous medium. The β-factor is the fraction of all the emitted photons that are emitted into the specific cavity mode. The latter is important for an efficient harvesting of light emission for a given purpose. It is of particular interest to couple the emitted photons into a guided mode [33, 34] that can lead the photons efficiently to the point of use.

4.1 Coupling to photonic crystal waveguides

We have experimentally investigated the coupling of single QDs to a PCM waveguide of the type W1 shown in Fig. 1(b) [22, 35]. In the membrane (150-nm thick) a single layer of InAs QDs is embedded with a density of $\sim 250\,\mu\mathrm{m}^{-1}$ and a ground-state emission wavelength around 960 nm. The QDs are excited from the surface in the μ-PL setup sketched in Fig. 2 by ~2-ps pulses from a Ti:sapphire laser emitting at 800 nm and strongly focused through a microscope objective with high numerical aperture (NA = 0.8). The QD exciton emission is detected through the same microscope lens with a resulting spatial resolution of 1.4 μm. The combination of the spatial resolution and the spectral resolution (0.15 nm) allows for the detection of single-QD emission lines from an ensemble of excited QDs with different positions and orientations with respect to the waveguide, and thereby possibly different couplings to it. This is reflected in the different intensities of the emission lines, but more distinctly in the measured radiative decay rate of the different lines. A large group of QDs show a slow decay that is well fitted with a single-exponential (decay rate $0.05\,\mathrm{ns}^{-1}$) representing a QD that is uncoupled to the waveguide and with a radiative decay strongly inhibited by the surrounding photonic crystal. Other QDs showed a faster decay well fitted by a bi-exponential decay. The fast component is representing the radiative decay coupled to the waveguide and the slow component is due to dark excitons as discussed in Section 3.2. The fast rate is up to 27 times faster than the uncoupled QD demonstrating that the QD emission can be coupled very efficiently to a PCM waveguide in agreement with recent theoretical proposals [33, 34].

A large number of measured decay rates on a sample with lattice constant $a = 256$ nm was analysed in Ref. [22] showing that the decay rate, and thereby the coupling to the waveguide, is increasing strongly as the frequency approaches the cut-off frequency of the PCM waveguide, *i.e.* as the group index increases in the slow-light region.

The coupling efficiency of the QDs to the PCM waveguide is quantified by the β-factor, which we can

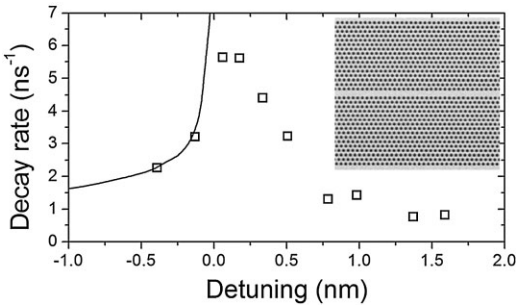

Figure 11 Measured QD decay rates (open squares) on a PCM W1-waveguide (inset) as a function of detuning from the waveguide cut-off wavelength at 969 nm. The solid curve is calculated from the simulated group velocity in a lossless waveguide.

calculate from

$$\beta = \frac{\Gamma_{\mathrm{wg}}}{\Gamma_{\mathrm{wg}} + \Gamma_{\mathrm{rad}} + \Gamma_{\mathrm{nrad}}} = \frac{\Gamma_{\mathrm{res}} - \Gamma_{\mathrm{non\text{-}res}}}{\Gamma_{\mathrm{res}}}, \qquad (9)$$

where Γ_{wg} is the decay rate into the waveguide mode, Γ_{rad} is the decay rate to non-guided modes, and Γ_{nrad} is the intrinsic nonradiative decay rate. Γ_{res} ($\Gamma_{\mathrm{non\text{-}res}}$) is the observed decay rate of a coupled (uncoupled) QD. In Ref. [22] it was found that the β-factor approaches 0.9 near the cut-off frequency of the waveguide. We have also varied the coupling of an individual QD to the W1 waveguide by temperature tuning the emission of the QD through the wavelength region around the cut-off wavelength of the waveguide [35]. The result is shown in Fig. 11 (open squares), from which again a high β-factor (0.85) can be deduced when the QD is resonant with the slow-light region of the waveguide. The decay rate of QDs coupled to a lossless PCM waveguide is calculated from the simulated group velocity [33] and is shown as the solid curve in Fig. 11. At resonance the enhanced decay rate corresponds to a Purcell factor $F_{\mathrm{p}} = \Gamma_{\mathrm{res}}/\Gamma_0 = 5.2$ where $\Gamma_0 = 1.1\,\mathrm{ns}^{-1}$ is the decay rate of the QD in a homogeneous medium. We have studied also a QD detuned by approximately -2 nm and found an almost constant decay rate of $\sim 2\,\mathrm{ns}^{-1}$. Thus, an efficient coupling to the PCM waveguide has been demonstrated over a bandwidth larger than 5 nm [35]. This is in contrast to the narrow bandwidth of efficient coupling to high-Q nanocavities [36, 37].

4.2 Influence of disorder It is obvious from the above that the radiative coupling of QDs to a PCM waveguide is strongly enhanced when the emission frequency approaches the waveguide cut-off frequency, *i.e.* in the slow-light region where not only the propagation of light is affected (velocity, dispersion), but where also losses, and in particular scattering (in the waveguide plane and out-of-plane) due to disorder, are increased. This poses a serious problem for an efficient coupling of the QD (single-photon) emission to an external user. However, it can also be considered as resource for an alternative way of localising light in very small-volume cavities. We have shown that

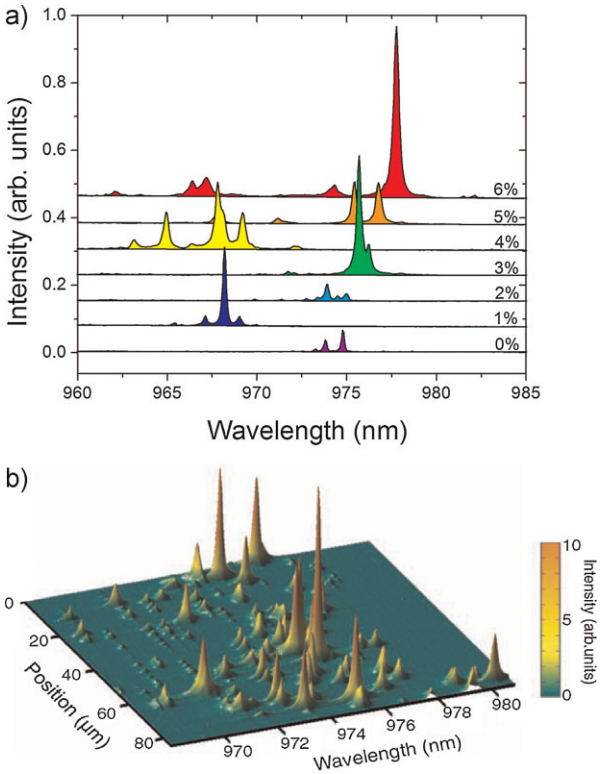

Figure 12 (online colour at: www.pss-b.com) (a) Spectra of Anderson-localised modes for different degrees of engineered disorder. The waveguide cut-off is at 978 nm. Each spectrum is collected with the excitation and collection microscope objective at a fixed position on the waveguide. The spectra are shifted vertically for visual clarity. (b) Scan along the waveguide for 3% disorder showing that the modes are indeed localised.

indeed Anderson localisation [38] of waveguide modes in such a PCM waveguide with controlled additional disorder can be obtained [39]. Figure 12(a) shows the spectral signature of such Anderson-localised modes. The localised modes are predominant near the cut-off wavelength of the waveguide. That they are indeed localised is shown in Fig. 12(b), where the microscope objective is scanned along the waveguide in a sample with 3% engineered disorder. It is interesting to speculate to what extent these disorder-localised modes can serve as an alternative to conventional nanocavities and open a new avenue towards all-solid-state cavity QED.

5 Applications Due to the discrete nature of the electronic states in QDs they are often called artificial atoms and it is the combination of the atomistic character and the fact that they appear in a solid-state environment that make them attractive for many applications. Devices based on semiconductor QDs can easily be incorporated in integrated and scalable photonic and electronic circuits, and devices containing single, or a few, QDs coupled to a nanocavity can be miniaturised to the smallest scale allowed by the wave nature of light [40]. This limit can be pushed further down if metallic (plasmonic) structures are incorporated [41].

The two-level nature of the ground-state transition of QD excitons ensures that transparency and gain (inversion) can be attained with very modest pumping, and the efficient coupling to nanocavities with high Q and small mode volume paves the way to very compact, low-threshold lasers [40] and switches. However, an efficient coupling off-chip remains a serious challenge.

Single QDs are ideal single-photon emitters from the ground-state transition [12, 42]. If the QD is excited further to obtain a significant biexciton population, it can even serve as an efficient source of entangled photon pairs [43]. The challenges are to obtain a high rate of photons, or photon pairs, on demand and also an efficient coupling to preferably an external optical fibre [44].

6 Conclusions We have performed extensive studies of self-assembled InAs/GaAs QD excitons placed in different nanostructured environments, *i.e.* with the refractive index varying on the wavelength scale. We have exploited the resulting variation in the LDOS to obtain direct experimental measurements of the quantum efficiency, oscillator strength and spin-flip rates of the QD excitons. We have further demonstrated that the spontaneous emission rate of QD excitons can be manipulated very effectively by placing the QDs in different environments. In PCMs the spontaneous emission rate is significantly inhibited for wavelength within the photonic crystal band gap. On the other hand, strong enhancement via the Purcell effect and an efficient coupling to localised modes in PCWs and nanocavities can be obtained. The influence of disorder in the PCW has been studied and Anderson localisation of waveguide modes has been observed. These investigations are essential for the further understanding and exploitation of QD excitons in nanophotonics devices.

Acknowledgements The authors gratefully acknowledge J. Johansen, T. Lund-Hansen, B. Julsgaard, H. Thyrrestrup, L. Sapienza, S. Smolka and P. D. Garcia for making their data available and T. Sünner, M. Kamp, T. Schlereth, S. Höfling and A. Forchel for growth and processing of samples. Thanks are due to the Danish Research Agency and the Villum Kann Rasmussen Foundation for financial support.

References

[1] H. Haug and S. W. Koch, Quantum Theory of the Optical and Electronic Properties of Semiconductors, second ed. (World Scientific, Singapore, 1993), p. 21.
[2] R. Loudon, The Quantum Theory of Light (Oxford University Press, Oxford, 2000).
[3] J. J. Hopfield, Phys. Rev. **112**, 1555 (1958).
[4] E. Gross, S. Permogorov, V. Travnikov, and A. Selkin, Solid State Commun. **16**, 1971 (1972).
[5] C. Weisbuch, M. Nishioka, A. Ishikawa, and Y. Arakawa, Phys. Rev. Lett. **69**, 3314 (1992).
[6] J. P. Reithmaier, G. Sek, A. Löffler, C. Hofmann, S. Kuhn, S. Reitzenstein, L. V. Keldysh, V. D. Kulakovskii, T. L. Reinecke, and A. Forchel, Nature **432**, 197 (2004).
[7] T. Yoshie, A. Scherer, J. Hendrickson, G. Khitrova, H. M. Gibbs, G. Rupper, C. Ell, O. B. Shchekin, and D. G. Deppe, Nature **432**, 200 (2004).
[8] A. Laucht, F. Hofbauer, N. Hauke, J. Angele, S. Stobbe, M. Kaniber, G. Böhm, P. Lodahl, M.-C. Amann, and J. J. Finley, New J. Phys. **11**, 023034 (2009).
[9] S. Reitzenstein, T. Heindel, C. Kistner, A. Rahimi-Iman, C. Schneider, S. Höfling, and A. Forchel, Appl. Phys. Lett. **93**, 061104 (2008).
[10] X. Ma and S. John, Phys. Rev. Lett. **103**, 233601 (2009).
[11] A. Imamoglu, D. D. Awschalom, G. Burkard, D. P. DiVincenzo, D. Loss, M. Scherwin, and A. Small, Phys. Rev. Lett. **83**, 4204 (1999).
[12] P. Michler, A. Kiraz, C. Becher, W. V. Schoenfeld, P. M. Petroff, L. Zhang, E. Hu, and A. Imamoglu, Science **290**, 2282 (2000).
[13] C. Schneider, A. Huggenberger, T. Sünner, T. Heindel, M. Strauss, S. Göpfer, P. Weinmann, S. Reitzenstein, L. Worschech, M. Kamp, S. Höfling, and A. Forchel, Nanotechnology **20**, 434012 (2009).
[14] K. Hennessy, A. Badolato, M. Wigner, D. Gerace, M. Atatüre, S. Gulde, S. Fält, E. L. Hu, and A. Imamoglu, Nature **445**, 896 (2007).
[15] A. Naesby, T. Suhr, P. T. Kristensen, and J. Mørk, Phys. Rev. A **78**, 045802 (2008).
[16] D. Birkedal, J. Bloch, J. Shah, L. N. Pfeiffer, and K. West, Appl. Phys. Lett. **77**, 2201 (2000).
[17] J. Johansen, S. Stobbe, I. S. Nikolaev, T. Lund-Hansen, P. T. Kristensen, J. M. Hvam, W. L. Vos, and P. Lodahl, Phys. Rev. B **77**, 073303 (2008).
[18] S. Stobbe, J. Johansen, P. T. Kristensen, J. M. Hvam, and P. Lodahl, Phys. Rev. B **80**, 155307 (2009).
[19] J. Johansen, B. Julsgaard, S. Stobbe, J. M. Hvam, and P. Lodahl, Phys. Rev. B **81**, 081304(R) (2010).
[20] P. Lodahl, A. F. van Driel, I. S. Nikolaev, A. Irman, K. Overgaag, D. Vanmaekelbergh, and W. L. Vos, Nature **430**, 654 (2004).
[21] B. Julsgaard, J. Johansen, S. Stobbe, T. Stolberg-Rohr, T. Sünner, M. Kamp, A. Forchel, and P. Lodahl, Appl. Phys. Lett. **93**, 094102 (2008).
[22] T. Lund-Hansen, S. Stobbe, B. Julsgaard, H. Thyrrestrup, T. Sünner, M. Kamp, A. Forchel, and P. Lodahl, Phys. Rev. Lett. **101**, 113903 (2008).
[23] C. Klingshirn, Semiconductor Optics, third ed. (Springer, Heidelberg, 2007), p. 392.
[24] J. Bellessa, V. Voliotis, R. Grousson, X. L. Wang, M. Ogura, and H. Matsuhata, Phys. Rev. B **58**, 9933 (1998).
[25] M. Sugawara, Phys. Rev. B **51**, 10743 (1995).
[26] S. Stobbe, T. W. Schlereth, S. Höfling, A. Forchel, J. M. Hvam, P. Lodahl, arXiv:1006.5796, resubmitted to Phys. Rev. B.
[27] E. Hanamura, Phys. Rev. B **37**, 1273 (1988).
[28] K. L. Drexhage, J. Lumin. **1-2**, 693 (1970).
[29] L. C. Andreani, G. Panzarini, and J.-M. Gérard, Phys. Rev. B **60**, 13276 (1999).
[30] O. Labeau, P. Tamarat, and B. Lounis, Phys. Rev. Lett. **90**, 257404 (2003).
[31] J. M. Smith, P. A. Dalgarno, R. J. Warburton, A. O. Govorov, K. Karrai, B. D. Gerardot, and P. M. Petroff, Phys. Rev. Lett. **94**, 197402 (2005).
[32] A. F. Koenderink, M. Kafesaki, C. M. Soukoulis, and V. Sandoghdar, J. Opt. Soc. Am. B **23**, 1196 (2006).

[33] V. S. C. M. Rao and S. Hughes, Phys. Rev. Lett. **99**, 193901 (2007).
[34] G. Lecamp, P. Lalanne, and P. Hugonin, Phys. Rev. Lett. **99**, 023902 (2007).
[35] H. Thyrrestrup, L. Sapienza, and P. Lodahl, Appl. Phys. Lett. **96**, 231106 (2010).
[36] A. Kress, F. Hofbauer, N. Reinelt, M. Kaniber, H. J. Krenner, R. Meyer, G. Böhm, and J. J. Finley, Phys. Rev. B **71**, 241304 (2005).
[37] W. H. Chang, W. Y. Chen, H. S. Chang, T. P. Hsieh, J. I. Chyi, and T. M. Hsu, Phys. Rev. Lett. **96**, 117401 (2006).
[38] P. W. Anderson, Phys. Rev. **109**, 1492 (1958).
[39] L. Sapienza, H. Thyrrestrup, S. Stobbe, P. D. Garcia, S. Smolka, and P. Lodahl, Science **327**, 1352 (2010).
[40] S. Strauf, K. Hennessy, M. T. Rakher, Y.-S. Choi, A. Badolato, L. C. Andreani, E. L. Hu, P. M. Petroff, and D. Bouwmeester, Phys. Rev. Lett. **96**, 127404 (2006).
[41] M. T. Hill, Y.-S. Oei, B. Smalbrugge, Y. Zhu, T. de Vries, P. J. van Veldhoven, F. W. M. van Otten, T. J. Eijkemans, J. P. Turkiewicz, H. de Waardt, E. J. Gelug, S.-H. Kwon, Y.-H. Lee, R. Nötzel, and M. K. Smit, Nature Photon. **1**, 589 (2007).
[42] A. J. Shields, Nature Photon. **1**, 215 (2007).
[43] R. M. Stevenson, R. J. Young, P. Atkinson, K. Cooper, D. A. Ritchie, and A. J. Shields, Nature **439**, 179 (2006).
[44] J. Claudon, J. Bleuse, N. S. Malik, M. Bazin, P. Jaffrennou, N. Gregersen, C. Sauvan, P. Lalanne, and J.-M. Gérard, Nature Photon. **4**, 174 (2010).